Multi-frequency MEMS Acoustic Emission Sensor

Talha Masood Khan, Raguez Taha, Tonghao Zhang and Didem Ozevin[*]

Department of Civil, Materials, and Environmental Engineering, University of Illinois Chicago
[*] Corresponding author, dozevin@uic.edu, 842 W Taylor Street ERF 2095 Chicago IL 60607

Abstract: In this paper, a multi-frequency MEMS acoustic emission (AE) sensor is designed, characterized, and tested. The sensor includes sixteen individual resonators tuned in the range of 100 kHz to 700 kHz. The resonator frequencies are selected to form constructive interference when they are connected in parallel to increase the signal-to-noise ratio. Each resonator is comprised of a membrane that forms the mass and four beams that provide stiffness. The membrane size is kept the same for each resonator to have approximately the same sensitivity per frequency. The influence of spring elements on the resonant frequency and the sensitivity is numerically demonstrated. The sensor is manufactured using MEMSCAP PiezoMUMPs. The characterization experiments show a slight shift in the resonant frequency of individual resonators compared to the design values. The MEMS sensor is packaged using a custom-designed printed circuit board to improve the signal-to-noise ratio. The sensor performance is compared with a conventional AE sensor. The sensitivity and frequency bandwidth of the MEMS AE device is brought to a comparable level to bulky AE sensors.

Keywords: MEMS, acoustic emission, multi-frequency, array, PiezoMUMPs

1 Introduction

The Acoustic Emission (AE) method is a passive nondestructive evaluation method that involves detecting high-frequency elastic waves (usually between 20 kHz and 500 kHz) generated by the rapid release of energy from sources within materials. AE sources can arise from materials-related factors, such as fatigue cracks or metal fiber breakage, or they can be externally generated through an impact. Detecting the target AE source properly requires carefully selecting an appropriate sensor, considering factors such as resonant versus broadband sensing, sensor size, frequency bandwidth, and sensitivity. For example, since concrete is an attenuative material, lower-frequency sensors (60 kHz – 200 kHz) are often selected to increase sensor spacing (Behnia et al., 2014, Appalla et al., 2016, Kawasaki et al., 2022). Additionally, the literature has shown that different failure modes in composites can be characterized by different frequency spectrums (Sause and Horn 2010, Karimian and Modarres 2021, Chen et al., 2021). Conventional broadband AE sensors are often able to cover the required frequency spectrum, but they tend to be both bulky and expensive.

MEMS AE sensors offer several advantages, including tuning the sensor to a specific frequency, designing multiple frequency sensors on the same device, cost reduction through batch fabrication, and applicability

to weight-restricted applications. In recent years, capacitive-type (Ozevin et al., 2006, Wright 2009, Saboonchi and Ozevin 2013, Avila Gomez 2017, Liu 2018, Butaud et al. 2020) and piezoelectric-type (Feng and Tsai 2010, Kabir et al. 2018, Kumar et al. 2019, Nastro et al. 2022, Qu et al. 2022) AE sensors have been designed, characterized, and tested. The main design variables are the resonant frequency, damping, and sensitivity. The piezoelectric MEMS AE sensors are formed by a silicon substrate with unique geometry at the target frequency and a piezoelectric layer. The motion of the silicon substrate introduces radial force, where the piezoelectric layer converts it into an electrical signal (Jia et al. 2021). The microstructure can be configured to tune each sensor to a particular resonant frequency (Ozevin 2020). Typical piezoelectric elements for thin film MEMS are ferroelectric (e.g., PZT) or non-ferroelectric (e.g., aluminum nitride (AlN) and zinc oxide (ZnO)) (Matsushima et al. 2012).

Current MEMS AE sensors have limited sensitivity and frequency ranges. However, Nastro et al. (2022) demonstrated that the resonant frequency of a piezoelectric MEMS AE sensor could be adjusted within a range of 5.4 kHz to 5.54 kHz by applying an electrical load of -8 V to 8 V. While this method allows for some degree of frequency tuning, the resulting change in the frequency band is still relatively small compared to the wide range of AE sources that can be detected from a single experiment as noted above. Chen et al. (2021) addressed this issue by configuring dual-frequency piezoelectric MEMS sensors using in-phase and out-of-phase modes, enabling detection at both 103 kHz and 220 kHz frequencies. Previous studies have explored piezoelectric MEMS arrays for ultrasonic transducers in square (Wang et al., 2008, Dausch et al., 2008, Wang et al., 2020) or rectangular (Lu et al., 2015, Liu et al., 2022) arrays. The common application for piezoelectric MEMS arrays is for medical imaging (Jung et al., 2017; Lee et al., 2021). These arrays typically consist of resonators tuned to the same frequency to increase sensitivity and resolution.

In the present study, an array of sixteen MEMS resonators with distinct frequencies in the range of 100 kHz to 700 kHz are connected in parallel to increase both sensitivity and frequency bandwidth. To simplify electrical wiring, the array is electrically connected during microfabrication, allowing all sixteen frequencies to be recorded through a single cable. The paper is organized as follows. Section 2 discusses the constraints of microfabrication on sensor design, while section 3 presents finite element analyses of the vibrational modes of MEMS sensors and sensitivity analysis. Section 4 outlines the optical and impedance measurements of the microfabricated sensors and face-to-face testing while section 5 describes the packaging of the sensor dies and the acoustic measurements in comparison to a conventional AE sensor. Finally, section 6 concludes with a discussion of the results obtained in this work.

2 Sensor Design Variables and Constraints

The MEMS AE sensors are manufactured using PiezoMUMPs provided by MEMSCAP. Manufacturing foundries have geometric and material constraints that govern the process of designing sensors for a specific application, and these geometric variables are provided in Table 1. Each resonator is comprised of a membrane that forms the mass and four beams that provide stiffness as shown in Figure 1. Membrane and beams are made of highly-doped silicon layer (Top Si) with a thickness constraint of 10±1 mm, minimum feature size of 2 μm. The piezoelectric element (Piezo layer) that transfers the kinetic energy into an electrical signal is Aluminum Nitride (AlN). The dimensional constraints for AlN are 0.5 mm thickness, and 3 μm as minimum feature length. Pad Oxide layer functions as an insulation between the metal layer (Pad Metal) and the Top Si layer and is 0.2±0.01 μm thick. The metal layer consists of a stack of chromium (Cr) and aluminum (Al) layers with thicknesses of 20 nm and 1000 nm, respectively. The total area of each chip is 5.575 mm x 5.575 mm; however, the usable area is limited to 4.5 x 4.5 mm due to a bonding process during microfabrication.

Table 1: Geometric variables of sensing elements (Cowen et al. 2014).

Geometric Variables	**Layer**	**Min feature size and spacing (μm)**	**Max feature length (μm)**	**Thickness (μm)**
Suspended Si	Top Si	2	Unlimited	10±1
Piezoelectric layer (AlN)	Piezo	10	5000	0.5
Metal Layer (Cr/Al)	Pad Metal	3	5000	1.02
Thermal Oxide	Pad Oxide	5	Unlimited	0.2
Buried Oxide	BOX	3	N/A	1
Bottom Substrate Silicon	Handle	200	5000	400

As shown in Figure 1, the metal layer connects the top of the piezoelectric layer to the top terminal. The same metal layer also connects the Top Si layer to the bottom terminal. Due to the presence of AlN only in the sensor's center, Pad Oxide separates the top and bottom terminals of the sensor on all four beams. The thickness of the central mass is 11.52 μm, while the thickness of all four beams is 11.22 μm.

Additional design constraints also limit the edge-to-edge bias and center-to-center overlay between different layers (Table 2). These design rules are dictated by microfabrication limitations. For example, Handle layer to Top Si edge-to-edge bias is a limitation used to account for the wet etch profile. Similarly, the edge-to-edge tolerance between the Pad Metal layer and the Piezo layer to the Top Si is defined to avoid masking during the dry etching process. This rule dictates that both the Pad Metal layer and Piezo layer should be enclosed by the Top Si layer on each side.

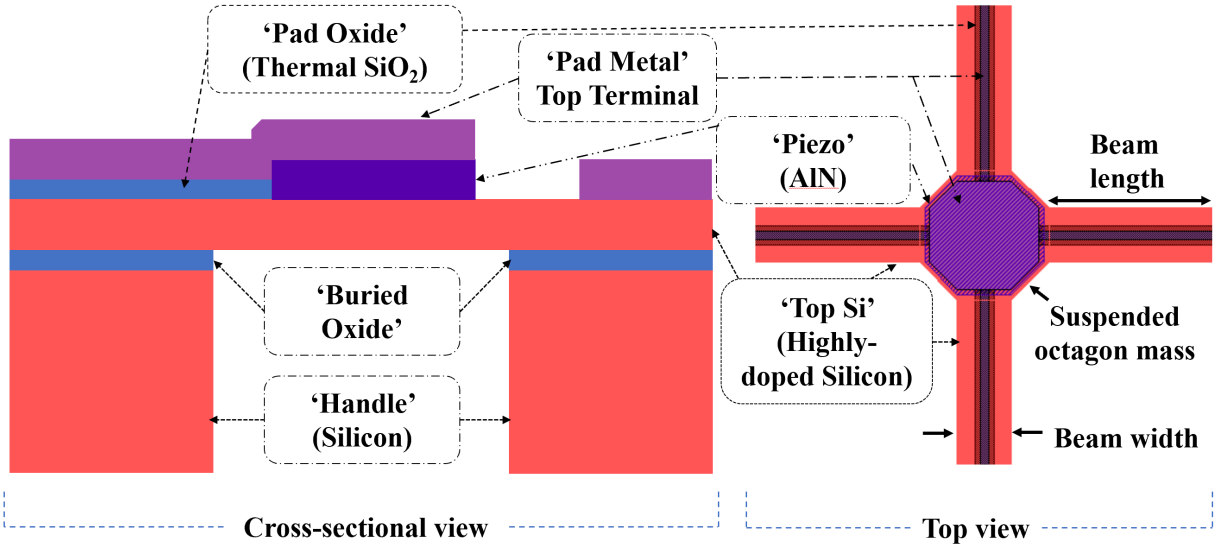

Figure 1: Illustration of an individual pMUT sensor. A cross-sectional view (left) and top view (right) of the sensor notate different layers from top to bottom. The top view also illustrates the variable lateral dimensions of the sensors.

The design objectives using these constraints are: (1) fitting sixteen resonators on a 4.5x 4.5 mm area, (2) selecting the frequencies to have constructive interference when they are connected in parallel, and (3) achieving similar sensitivity for each resonator. To have similar sensitivity, the total area of the Piezo layer is kept the same by keeping the diameter of the octagonal central mass the same as 300 µm. An octagon shape is selected instead of circular shape to reduce the microfabrication issues related to the digitization of image when printing the photolithographic masks. The cantilever beam length is varied to control the fundamental frequency, which is extracted from the numerical simulations discussed in the next section.

Table 2: Layer to Layer constraints of pMUT sensors elements. (Cowen et al. 2014)

Layer Stack	**Center-to-Center Overlay Tolerance (µm)**	**Edge-to-Edge Bias (µm)**
Piezo Layer to Top Si	± 5	± 5
Pad Metal Layer to Top Si	± 3	± 3
Handle Layer to Top Si	± 5	<50

Figure 2 shows the final design layout in a multi-mask layout design software (Tanner, L-Edit, Tanner Research Inc. USA). Sixteen resonators with the frequency range of 100 kHz to 700 kHz could be arranged according to the design constraints shown in Table 2. They are connected using two configurations: each

resonator has its own top electrode to be able to connect individually (Layout 1), and all resonators are electrically connected in parallel on the chip level (Layout 2). Layout 1 (L1) enables the characterization of the electromechanical properties of each resonator. Layout 2 (L2) reduces the number of wire bonding and cabling needed for all sixteen resonators to function as a single-channel AE array sensor. L1 has one top electrode and one bottom electrode to pin out each individual sensor. L2 has one top and one bottom electrode to pin out the parallel connected array, with additional redundant electrodes. Both layouts are designed to be contained in a 4.5 x 4.5 mm space with an active area of 5.0 x 5.0 mm.

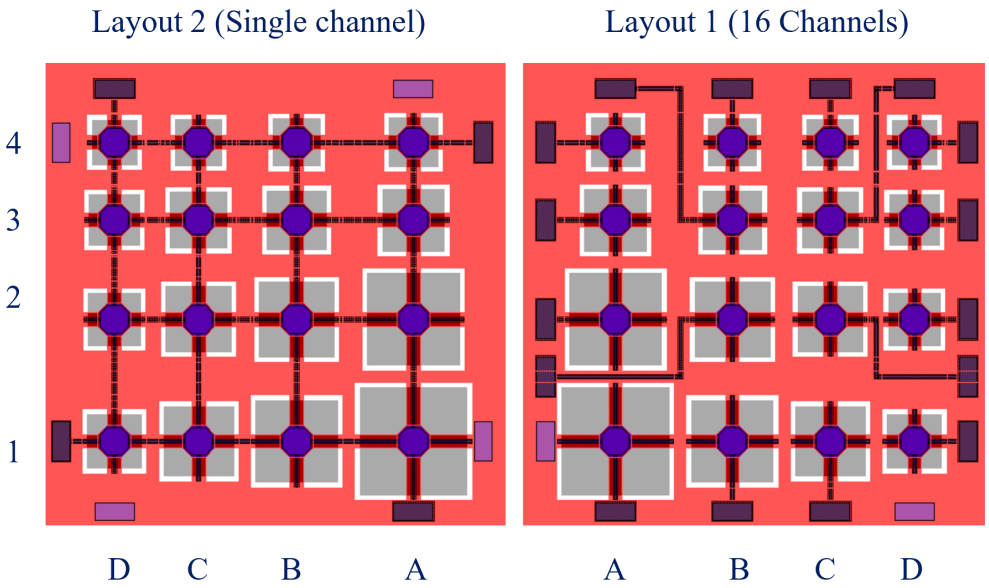

Figure 2: The top views of the final design layouts. Layout 2 with sixteen sensors connected in parallel (left), Layout 1 with sixteen individually placed sensors (right).

3 Numerical Simulations

3.1 Vibrational Modes

A single resonator is composed of a central octagonal membrane that is suspended by 4 edge-clamped beams on four sides. The central membrane consists of a piezoelectric layer sandwiched between a metal stack and silicon layer, as shown in Figure 1. Each beam has a silicon layer at the bottom, with an oxide and metal stack on top of it. The finite element model (using COMSOL 5.4, COMSOL Inc.) is established by clamping each of the beams on the outer edges. Material properties of Si and AlN layers used in the numerical models are listed in Table 3 (Cowen et al. 2014, Setter et al. 2006, Dubois and Muralt 1999, Gillan 2013).

Following the dimensional constraints presented in Table 1, each resonator is designed by fixing the beam width and the octagon side length (125 µm) while varying the beam length. The central mass of the

membrane is 1.95 mg. Sixteen individual frequencies are chosen from 100 kHz to 700 kHz with a 40 kHz step size. An eigenvalue analysis for each resonator is performed. A free tetrahedral mesh is selected for this simulation, with the mesh size set to fine.

Table 3: Materials properties of mass, spring, and sensing elements.

Material	**Young's modulus E (GPa)**	**Density ρ (kg m^{-3})**	**Poisson's ratio ν**	**Piezoelectric coefficient d_{33} (pC/N)**	**Melting point (°C)**
Si for mass and spring	156	2,330	0.125	-	1414°C
AlN for sensing	320	3,300	0.24	3.4-6.5	2830°C

The fundamental frequencies of all 16 resonators are shown in Figure 3. For low-frequency sensors (e.g., 100 kHz), the resonators' fundamental mode shapes exhibit uniform deformation in radial directions because of their longer beam lengths. However, shortening the beam lengths to increase the fundamental frequency leads to a non-uniform stress distribution, which can affect the conversion of mechanical vibration into an electrical signal as discussed in the next section.

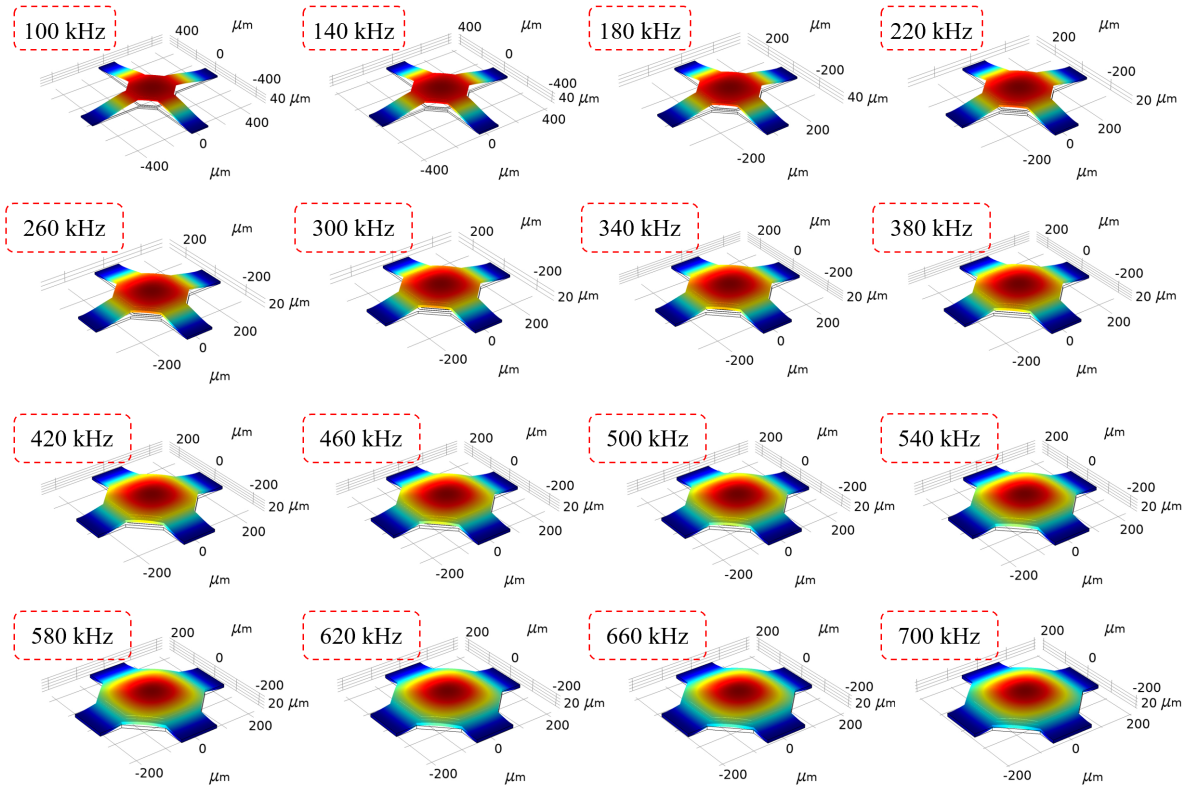

Figure 3: The fundamental mode shapes of sixteen resonators with varying beam lengths. The frequency range varies from 100 kHz to 700 kHz with a 40 kHz step.

Figure 4 depicts the second and third mode shapes of the resonator with a fundamental frequency of 100 kHz. The second and third mode frequencies are 257.03 kHz and 257.04 kHz, respectively. As the opposing deformations produced on the piezoelectric layer cancel out the electrical currents produced by the 2nd and 3rd mode shapes, they are not considered in the sensitivity calculations. Similar behavior occurs for higher-order modes; therefore, only the first mode is used to characterize the behavior of each resonator.

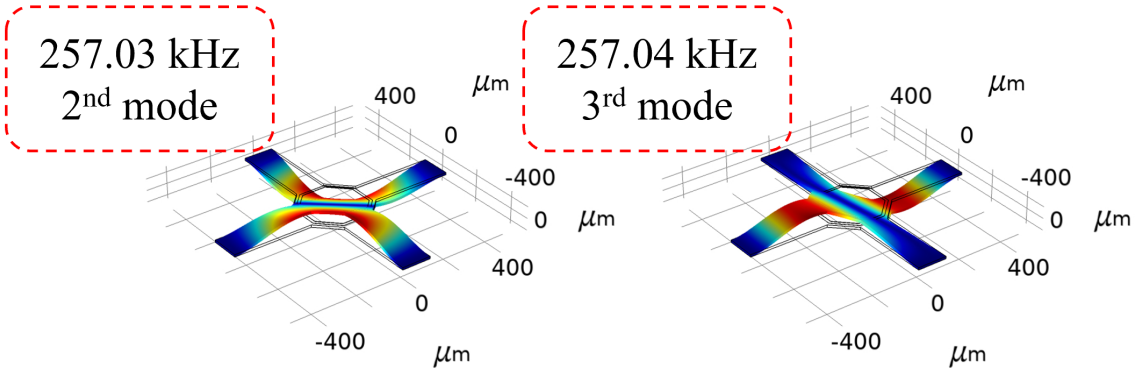

Figure 4: The second and third mode shapes of the lowest frequency (100 kHz) resonator.

3.2 Relative Sensitivity Analysis of Resonators

The sensitivity of thin film piezoelectric sensors differs from that of bulk piezoelectric sensors, as it is influenced by the material and structure of the substrate on which the piezoelectric film is deposited. Specifically, the out-of-plane motion of the silicon substrate causes in-plane expansion of the piezoelectric thin film, resulting in the generation of an electrical signal. The effective transverse piezoelectric coefficient describes the sensitivity of MEMS AE sensors produced with thin piezoelectric film on a membrane-type substrate (Dubois and Muralt 1999). The effective piezoelectric coefficient, $e_{31,f}$, of thin films, is calculated by $e_{31,f} = \frac{d_{31}}{s_{11}^E + s_{12}^E}$, where s_{ij}^E is the elastic compliance coefficient (Chun et al. 2013). The electrical displacement, D_3, is related to $e_{31,f}$ and strains in two directions as the third direction strain is zero due to free surface: $D_3 = e_{31,f} \times (\varepsilon_1 + \varepsilon_2)$.

As discussed earlier, the areas of the piezoelectric layer and membrane (i.e., mass) are kept the same for all the sensors, while their beam lengths (i.e., stiffnesses) are varied depending on the target frequency. As the membrane has an octagon shape and the strain transfer from the membrane to the piezoelectric layer does not have an analytical solution, the effective piezoelectric coefficients relative to the stiffnesses of the sensors are numerically calculated. A stationary model is designed with varying resonating frequencies that depend on the length of the beam. The center mass is suspended by four edge-clamped beams situated on top of the Handle layer, while a free tetrahedral mesh with a fine mesh size is used for the top layers and a

coarse mesh size for the Handle layer. A fixed boundary constraint is applied to the bottom of the Handle layer. As the sensors convert the inertial force into a current, a uniform distributed load of $1\ N/m^2$ is applied on the membrane in z direction leading to a deformation in z direction as shown in Figure 5. The total radial force produced on the piezoelectric thin film is calculated by integrating radial stress, σ_{rr} over total electrode area. The conversion of cartesian stresses into radial stress is achieved by

$$\sigma_{rr} = \sigma_{xx}cos^2\theta + \sigma_{yy}sin^2\theta + \sigma_{xy}sin2\theta \quad (1)$$

Where σ_{xx} is the stress tensor in the x direction, σ_{yy} is the stress tensor in the y direction, σ_{xy} is the stress sensor in the x-y direction, and θ is the angle in the x-y plane.

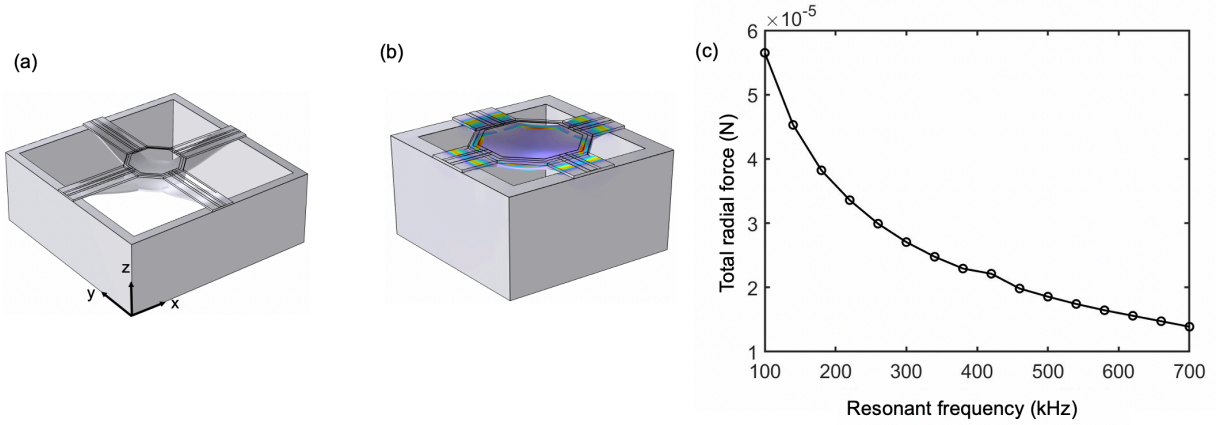

Figure 5: The numerical model to calculate the total radial force on the piezoelectric element, (a) the deformed shape of the 100 kHz resonator, (b) the deformed shape of the 700 kHz resonator, and (c) the total radial force produced on each resonator.

Figure 5(a) and (b) depict the deformed shapes of the lowest and highest frequency resonators. As expected, the lowest frequency resonator exhibits higher displacement due to its lower stiffness. With an increase in resonant frequency, stiffness increases, causing the total radial forces generated on the piezoelectric film to decrease. It is worth noting that the total force shown in Figure 5(c) is due to static loading. The resonators amplify the static displacement, resulting in a dynamic amplification factor when dynamic loading coincides with the membrane's resonant frequency. Considering the only fundamental mode, each resonator can be modeled as a single-degree-of-freedom system. The maximum dynamic displacement, $u_{o,n}$, when the input frequency matches the resonant frequency of resonator n, is calculated (Chopra 2019)

$$u_{o,n} = \frac{u_{st,n}}{2\zeta_n} \quad (2)$$

Where $u_{st,n}$ is static displacement and ζ_n is the damping ratio of resonator n obtained using the half-power bandwidth method applied to the impedance measurement in section 4.2. The total radial force shown in

Figure 5(c) is amplified by $1/2\xi_n$. The total current produced by each resonator is proportional to the piezoelectric coefficient and the total dynamic force exerted on the piezoelectric film. While the total area of the piezoelectric layer is kept the same for all resonators, their output charge produced due to a wideband excitation signal may differ. In future work, the membrane size and beam length will be varied to maintain the same sensitivity per resonator.

4 Characterization Experiments

4.1 Dimensional Inspection of MEMS AE Sensor

After the microfabrication process, each die is visually inspected using an optical microscope (Keyence VHX6000). To evaluate the changes in dimensions, the microscope is configured in normal mode (0^o) to measure lateral dimensions (length and width) and tilted mode (60^o) to measure vertical dimensions (thickness). All four beams of each sensor (top, bottom, left and right) are designed to have equal lengths and widths. Figure 6 shows the beam length, beam width, and the cross-length of the central mass of the resonator designed at 460 kHz. The inset also shows that the thickness of the beam is near 11 µm which coincides with the designed thickness of the beam.

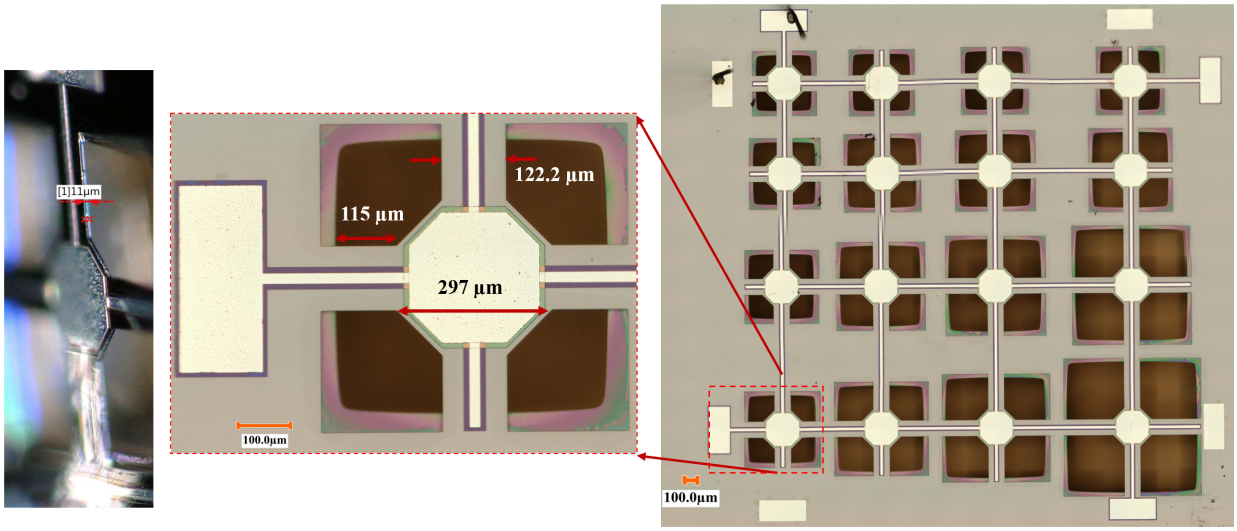

Figure 6: The dimensions of the resonator at the 460 kHz design frequency and the optical image of Layout 2.

Table 4 shows the comparison between the design and measured values of beam width and the octagon's central length. Lateral dimensions for all 16 sensors on both Layout 1 and Layout 2 were measured for comparison. These measurements show that the MEMSCAP process has over-etching on both Top Si and Handle layers, which causes changes in the design dimensions. Due to the over-etching of the Handle layer, the length of each edge-clamped beam increases. This increase can be proportional to the total etched area

of the underlying Handle layer. Over-etching in the Top Si layer causes a decrease in beam width. It should also be noted that there is a slight misalignment due to backside alignment that caused the length of the left beam of each sensor to be slightly larger than the length of the right beam. This difference amounts to a percentage difference of 6.54% with a variance of 6.67% for all 16 sensors on the die L2. Top and bottom beams also have this misalignment difference; however, it is not as significant. The measured length of the octagon membrane has also been altered such that the average for all 32 sensors on L1 and L2 is 297.3 μm in comparison to the designed length of 300 μm with a variance of 3.99 μm. The average measured beam width is 122.53 μm which is less than the designed length of 125 μm. The difference between the designed beam length and the measured average beam length varies between 13.38 to 20.6 μm. A trend of decrease in the difference in beam length with the increase in resonance frequency is also observed. However, even when the difference from the designed beam length is higher for lower frequencies, the percentage change in length is lower in comparison to the percentage change in higher frequencies. For the 100 kHz resonator, the percentage difference (measured vs design) in beam length is 5.38%, while it is 27.41% for the 700 kHz resonator. Owing to these issues, changes in the fundamental frequencies of resonators are observed and discussed in the following section.

Table 4: Beam width and octagon length's averages and standard deviations for all the resonators in Layout 1 and Layout 2

Variable	**Design**	**Measurement (Avg)**	**Measurement (Std-Dev)**
Beam width (μm)	125	122.53	0.438
Octagon length (μm)	300	297.3	1.997

4.2 Impedance Measurements

An impedance analyzer (Agilent Technologies, 4294A Precision Impedance Analyzer) is used to measure the admittance of individual (L1) and array (L2) configured MEMS AE sensors. Admittance is measured by sweeping frequency from 50 kHz up to 800 kHz. The sweeping range is segmented to enhance the measurement's sampling rate. These measurements are then concatenated to show all 16-resonance frequencies in Figure 7. The inset shows a close-up view of impedance measurement for the resonator at 380 kHz. Several parameters, frequency, bandwidth, and damping ratio of fundamental mode for each resonator, n, are extracted based on the admittance data collected. The resonant frequency, f_n, is extracted by reading the frequency at the peaks in Figure 7. The frequency bandwidth, Δf, is calculated as the change in frequencies to the right, $f_{right,n}$, and left, $f_{left,n}$, which correspond to the frequencies at 0.707 times the peak response of the phase (Kabir 2018). The quality factor, Q, is calculated using the half-power bandwidth method and is estimated as the ratio of the resonant frequency and the frequency bandwidth (Kabir 2018).

The damping ratio, ζ_n, is calculated as the ratio of the bandwidth and twice the resonant frequency. The effective electromechanical coupling coefficient, k_n^2, represents the total electrical energy that is converted to mechanical energy or vice versa. It is derived from the passive and motional capacitance, $C_{o,n}$ and $C_{m,n}$, respectively, and can also be determined using the resonance and antiresonance peaks of individual sensors (Birjis 2022). Passive capacitance is estimated, $|Y_n| \cong \omega_n C_{o,n}$, using the admittance values at off-resonance (Bhugra 2017).

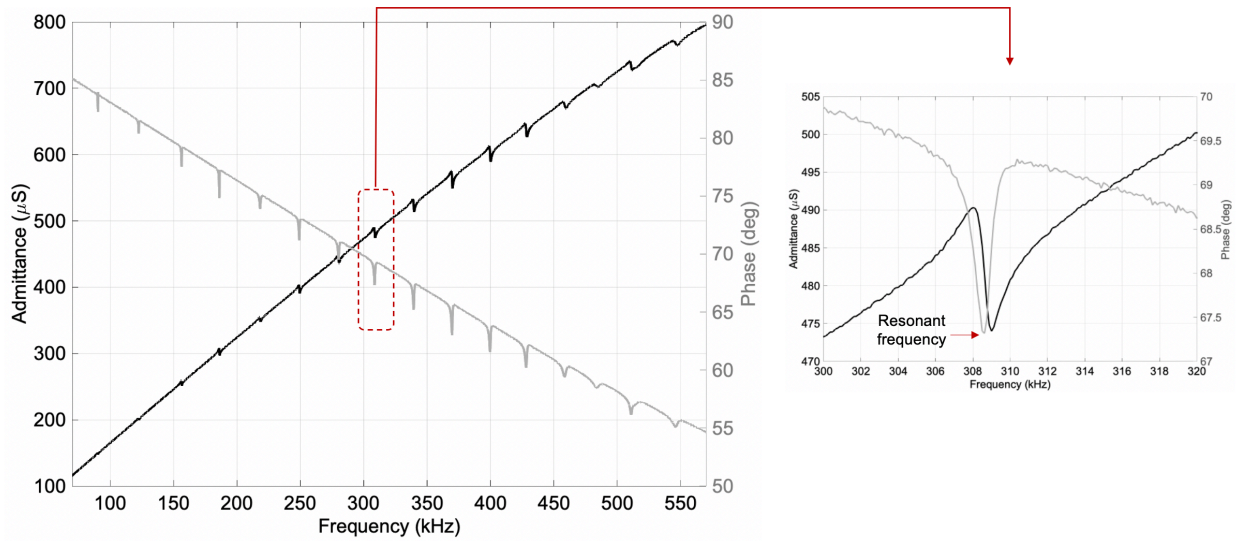

Figure 7: Admittance measurement of parallel connected resonators (L2). The inset shows the admittance of the resonator with the design frequency of 380 kHz.

Table 5: Electromechanical properties of pMUT sensors.

Resonator	**Design f_n (kHz)**	**Measured f_n (kHz)**	**Bandwidth (kHz)**	**Damping ratio (ζ) $\times 10^{-3}$**	**Electromechanical coupling coefficient (k^2) $\times 10^{-3}$**
A1	100	90.38	0.25	1.35	27.21
A2	140	122.50	0.22	0.88	20.10
B1	180	156.38	0.29	0.94	15.94
B2	220	186.13	0.35	0.93	13.29
C1	260	218.24	0.63	1.44	11.40
C2	300	249.13	0.52	1.04	9.93
A3	340	280.21	0.68	1.21	8.87
B3	380	308.61	0.65	1.06	8.05
C3	420	339.38	0.68	1.00	7.29
D1	460	369.64	0.63	0.86	13.33

D2	500	399.63	0.77	0.97	6.20
D3	540	428.13	0.95	1.11	5.79
A4	580	458.48	1.54	1.68	10.84
B4	620	484.13	2.07	2.14	35.49
C4	660	510.89	1.14	1.12	23.89
D4	700	545.88	2.23	2.05	9.09

Table 5 summarizes the parameters calculated from the impedance data. The results indicate that the bandwidth of resonators increases with the increase in frequency. This can be attributed to the decrease in beam lengths when compared to fixed central mass. The resonators exhibit an average damping ratio of 0.0012 with a standard deviation of 0.0004. As the admittance measurements are performed for both layouts L1 and L2, they are plotted against the design frequencies in Figure 8. The measured-to-design frequency ratios for L1 and L2 are 75.8% and 74.2%, respectively. A perfect curve fit between the design and measured frequencies could indicate a difference in material properties used in the numerical models and a misalignment of the mask that affects the lengths of all the resonators in a similar way. The difference between L1 and L2 is attributed to changes in dimensions caused by microfabrication and additional stray elements in the array configurations.

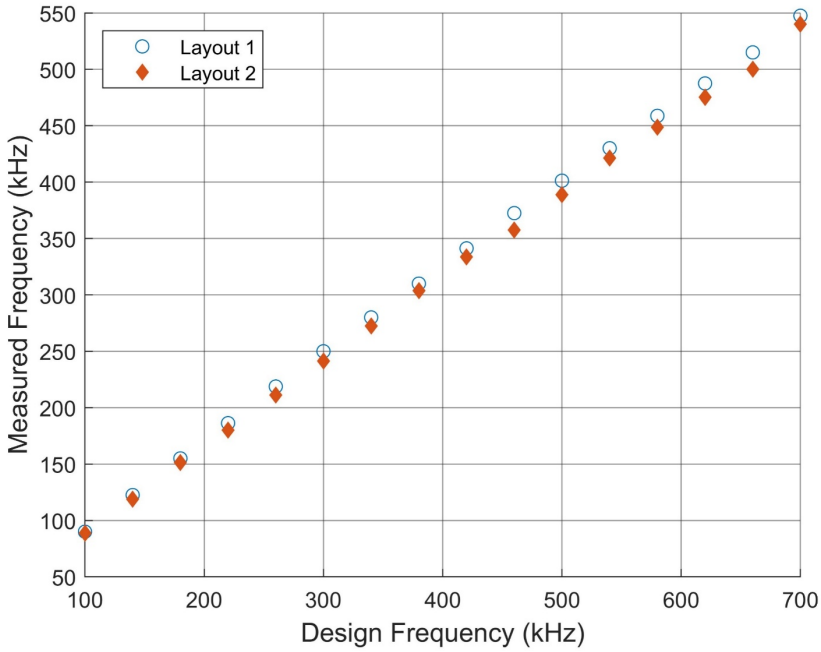

Figure 8: The comparison of the design and the measured frequencies.

To determine whether the shift in resonance frequency is caused by changes in physical dimensions, the lateral dimensions of resonators measured from the optical images are used to model the resonance frequency. The numerical results of two resonators with the actual dimensions reveal a similar trend where the resonance frequency decreases as compared to the design dimensions. Table 6 shows the fundamental frequencies for the lowest and highest frequency resonators. New results closely match the measured resonance frequency for the lower frequency sensor as compared to the higher frequencies. As low-frequency resonators have longer beams, slight changes in their lengths do not significantly affect their frequency. For instance, a change in beam length from 340 to 360.6 μm for the 100 kHz resonator only results in a small percentage change of 6.05%. However, a change in beam length from 55 to 69.38 μm for the 700 kHz resonator constitutes a substantial percentage change of 26.2%. Therefore, even a small measurement error when measuring the length of high-frequency resonators can cause a significant shift in frequency when evaluating using these dimensions in COMSOL.

Table 6: Comparison of design and measured resonance frequencies for highest and lowest frequency sensor as well as simulated resonance frequency with actual measured dimensions.

Resonator	**Numerical model with the design dimensions (kHz)**	**Measured using impedance analyzer (kHz)**	**Numerical model with the measured dimensions (kHz)**
A1	100	90.38	91.12
D4	700	545.75	617.78

4.3 Face-to-face Testing

MEMS sensors are initially housed in a commercially available leaded ceramic package (CCF02822-Spectrum semiconductor materials) for benchmark testing. To secure both L1 and L2, a non-conductive epoxy is used to attach them to the bottom of their respective packages, followed by wire bonding. Face-to-face testing is performed using an F15 as transmitter while the receiver is R15, MEMS L1 or MEMS L2 (one of individual resonators), as shown in Figure 9. A MISTRAS PCI-8 system with the frequency up to 400 kHz is used to perform this test. A chirp signal between 100 kHz to 400 kHz is generated with an amplitude of 1 V. As the ceramic package is exposed to higher electromagnetic noise, the analog frequency filter is set as 100 kHz to 400 kHz for all the sensors.

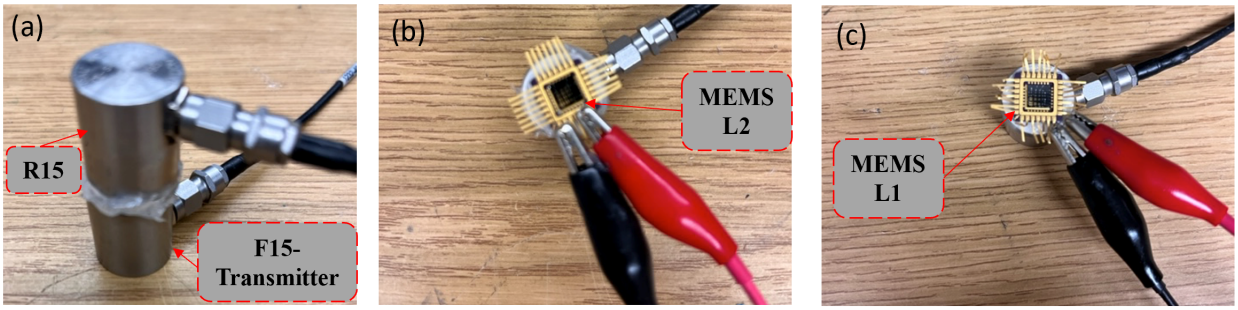

Figure 9: Face-to-face testing with F15 as transmitter and (a) R15, (b) MEMS L2 and (c) MEMS L1 as receiver.

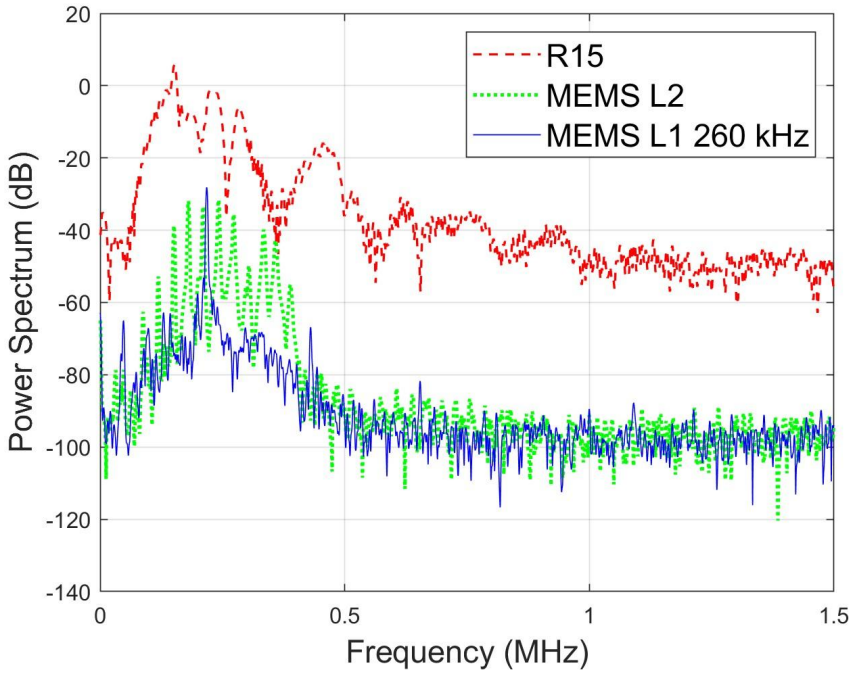

Figure 10: Power spectrums for (a) R15, (b) L2, (c) L1 with sensor C1 with resonance at 260 kHz.

Figure 10 shows the power spectrums of three sensors. The MEMS resonator C1, operating at 260 kHz, is chosen as the sensor for the MEMS L1 configuration. A slight reduction in the amplitude of the MEMS L2 resonator at 260 kHz is observed compared to the individual resonator of 260 kHz on MEMS L1. This difference is attributed to the parallel connection of the MEMS resonators in the MEMS L2 design. In general, MEMS AE sensors exhibit a sensitivity that is approximately 10 dB to 40 dB lower than that of R15, a reference sensor. Despite having lower sensitivity, MEMS L2 has the advantage of being smaller in size and weight compared to bulky conventional AE sensors. It is worth noting that the aperture size of an F15 transmitter is larger than the size of the MEMS sensors. Therefore, the signal generated by the F15 to trigger the MEMS sensors is expected to be lower than that of R15. Another source for lower response for the MEMS AE sensors is electronic impedance mismatch. To ensure that no signal loss occurs between the

sensor and the pre-amplifier due to impedance mismatch, an additional impedance matching configuration is necessary between the MEMS AE sensor and the pre-amplifier, which will be investigated as future work.

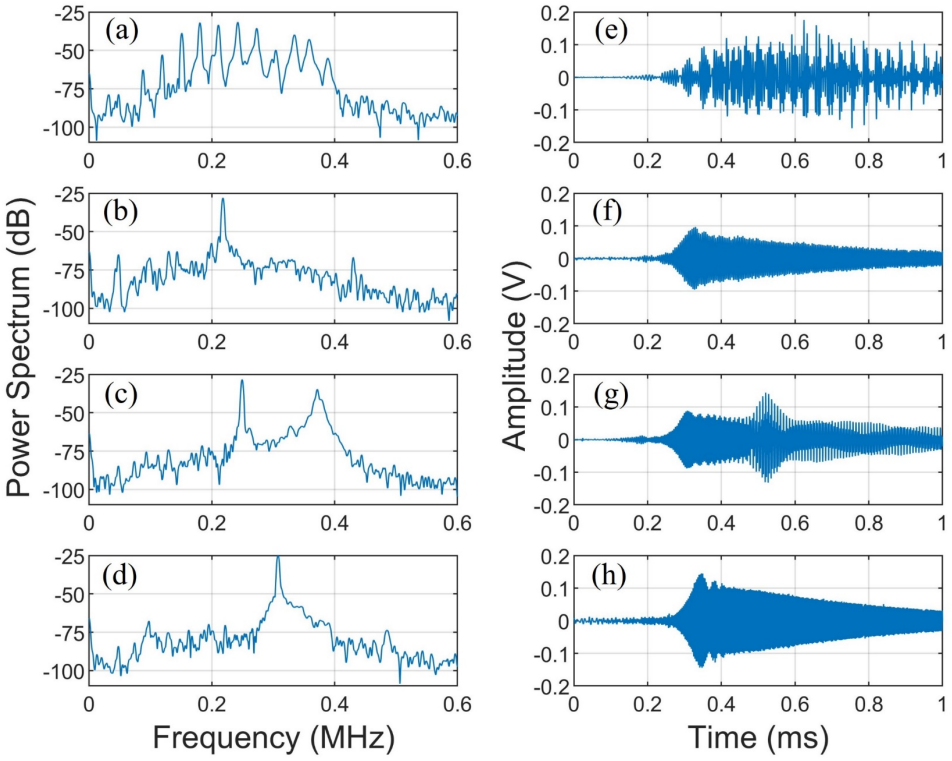

Figure 11: Power spectrums (a-d) and time history (e-f) signals for MEMS sensors. Outputs for MEMS L2 is shown in (a) and (e). Outputs for individual sensors in MEMS L1 with design frequency at 260 kHz is shown in (b) and (f), 300 kHz in (c) and (g) and 380 kHz in (d) and (h).

Figure 11 presents the time history signals of MEMS L2, MEMS L1 at 260 kHz (C1), 300 kHz (C2), and 380 kHz (B3) to demonstrate the improvement in signal-to-noise ratio (SNR) achieved through the combination of sixteen resonators. Each individual element in the array exhibits a peak near 25 dB at its respective resonance frequency, indicating the resonators' ability to detect and amplify signals at those specific frequencies. However, it is important to note that alongside the desired peak response, some reflections are observed in the signals due to near field effect and wave interference between transmitter and receiver. While these reflections contribute to the overall signal, they can also introduce interference and influence the overall SNR of the system. In the case of sensor C2 designed at 300 kHz, a particularly strong reflection is observed, resulting in a higher amplitude in the signal and a secondary frequency near 400 kHz. Despite the presence of reflections, the amplitude of MEMS L2 is significantly higher compared

to MEMS L1 at 260 kHz. This substantial increase in amplitude can be attributed to the constructive contributions of the resonators in the array, which work together to add to the output signal.

The improved and reserved SNR achieved with the combination of sixteen resonators highlights the effectiveness of the array design in enhancing the detection capability of the MEMS sensors. By leveraging the collective response of multiple resonators, the array not only amplifies the target signal but also detects multiple frequencies at the same time, which can be used for signal classification and pattern recognition.

5 Packaging and Acoustic Emission Performance

5.1 MEMS Package using Custom-designed Printed Circuit Board

Sensor packaging is necessary to pin out the connections from the die to the acquisition system and to ensure good acoustic matching between the sensor substrate and the structure to which the sensors are being coupled. Two printed circuit board (PCB) plates are used to enclose the die. This consists of a thin bottom lid (0.396 mm) and a thick top lid (3.175 mm), as shown in Figure 12. This PCB is also designed to reduce the level of the noise for measurement purposes. An SMA jack connector is soldered through the top lid such that it contacts the bottom lid through drilled holes. The sensor die is placed and fixed on the bottom lid using epoxy. The top and bottom contacts are then wire bonded before the top lid is placed. The bottom lid is then bent around all edges and sealed using a non-conductive epoxy. The packaged sensor is shown in Figure 13 with an external SMA plug connecting to the digital acquisition system discussed in section 5.2. The weights of R15 and MEMS package are 36.3 gram and 3.63 gram, respectively. Having a smaller sensor in a lighter packaging makes the application of AE method well suited for weight-limited applications, such as aerospace structures.

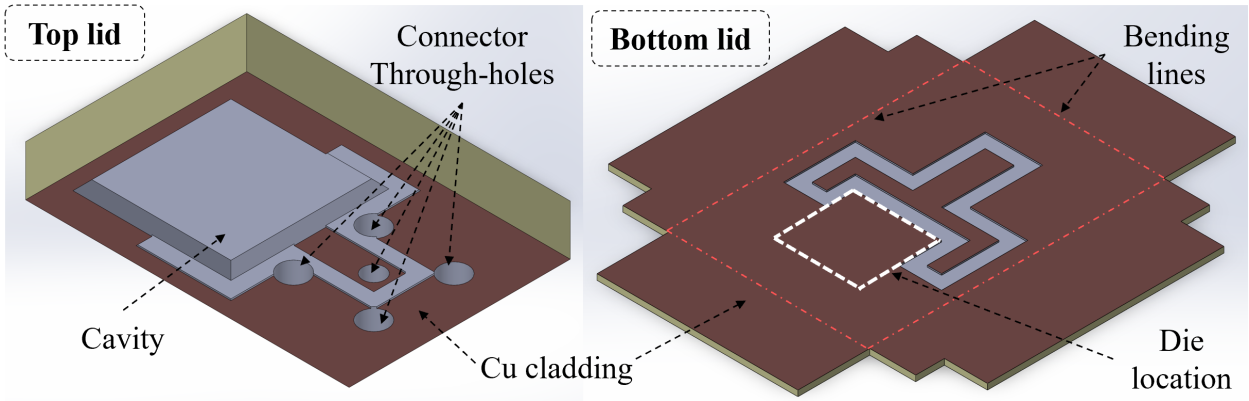

Figure 12: SolidWorks design for the top and bottom lids of MEMS packaging. The thick top lid consists of a cavity to accommodate space for the sensor die, and the wire bonds that are placed on a thin bottom

lid. The connector is soldered to the through holes in the top lid, where they contact the bottom lid once they are sealed together.

5.2 Sensitivity of Single Channel Configuration (L2 Layout)

The sensitivity of the MEMS AE sensor is compared with the conventional bulky AE sensor using pencil lead break (PLB) as the AE source. The selected bulky AE sensor is R15 (resonant type sensor with a resonant frequency of 150 kHz and a frequency bandwidth of 50 kHz to 400 kHz), manufactured by MISTRAS Group. Both sensors are connected to the PCI-2 data acquisition system. The sensors are coupled on a composite plate using vacuum grease, as shown in Figure 13. The PLB simulations are conducted on the top and bottom surfaces of the composite plate.

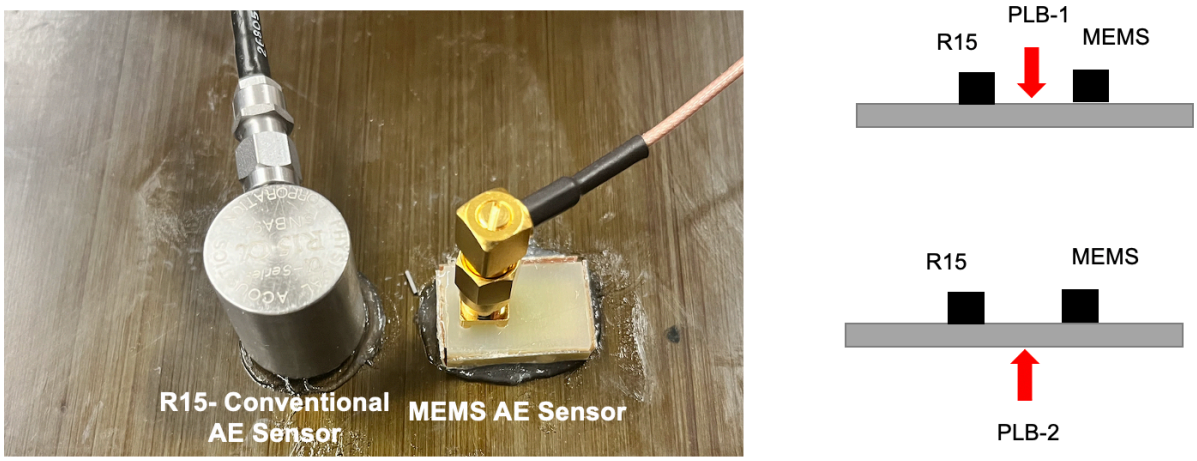

Figure 13: The AE simulation experiments to compare the sensitivity of the MEMS AE sensor with the bulky AE sensor.

Figure 14 shows the time history signals of R15 and MEMS sensors when the simulations were conducted parallel and orthogonal to the sensor area. When all the frequencies are considered, the outputs of the MEMS sensor are about 10-20 times smaller than the bulky AE sensor. The signal loss occurs due to the acoustic impedance difference between the packaging material of the MEMS AE sensor and composite, while the package significantly improved the electronic noise as compared to those reported in the literature. The ring-down time for the MEMS AE sensor is longer due to the lower damping coefficient, which can be increased by adding backing material.

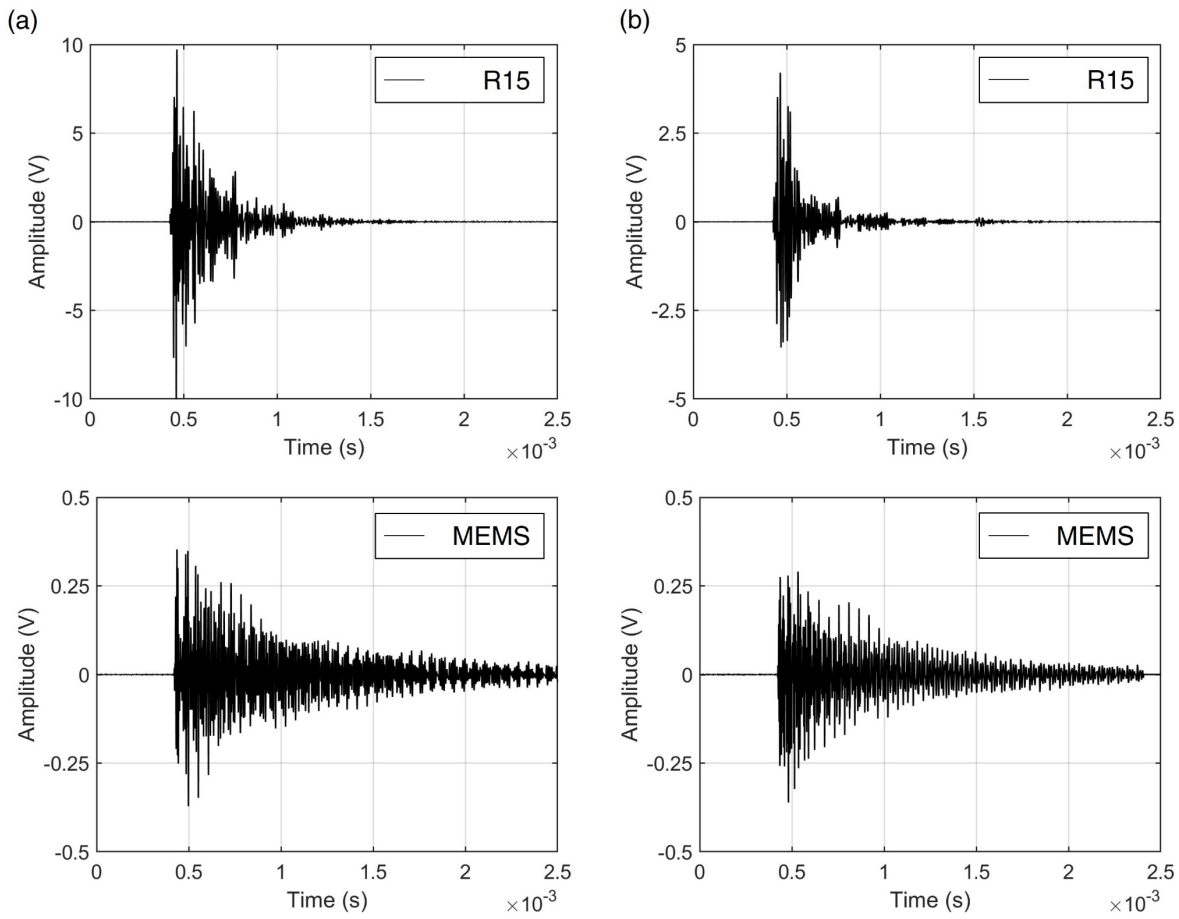

Figure 14: The AE signals recorded by R15 and MEMS when the PLB simulations are conducted on (a) the top surface, parallel plane as the sensor area (PLB-1), and (b) the bottom surface, orthogonal to the sensor area (PLB-2).

Figure 15 compares the frequency spectra of two sensors and two simulations. The peak frequency near 150 kHz shows that the R15 sensor has a higher output than the MEMS AE sensor by approximately 10 dB. However, the MEMS AE sensor can detect higher frequencies with higher amplitude when the direction of the AE source with respect to the sensor area is changed from parallel to orthogonal. The principle of the MEMS AE sensor is based on the radial force introduced to the piezoelectric layer due to the inertia force, as discussed earlier. Therefore, the MEMS AE sensor produces a higher output signal for pressure waves (simulated by PLB-2) compared to surface waves (simulated by PLB-1). The distinct output characteristic of the MEMS AE sensor, which varies depending on the wave mode, can be used to differentiate AE sources at different planes. As shown in the sensitivity analysis in section 3.2, low-frequency resonators exhibit higher sensitivity than high-frequency resonators. It is also observed from the excitation experiments that resonators below 300 kHz have higher amplitudes as compared to high-frequency resonators.

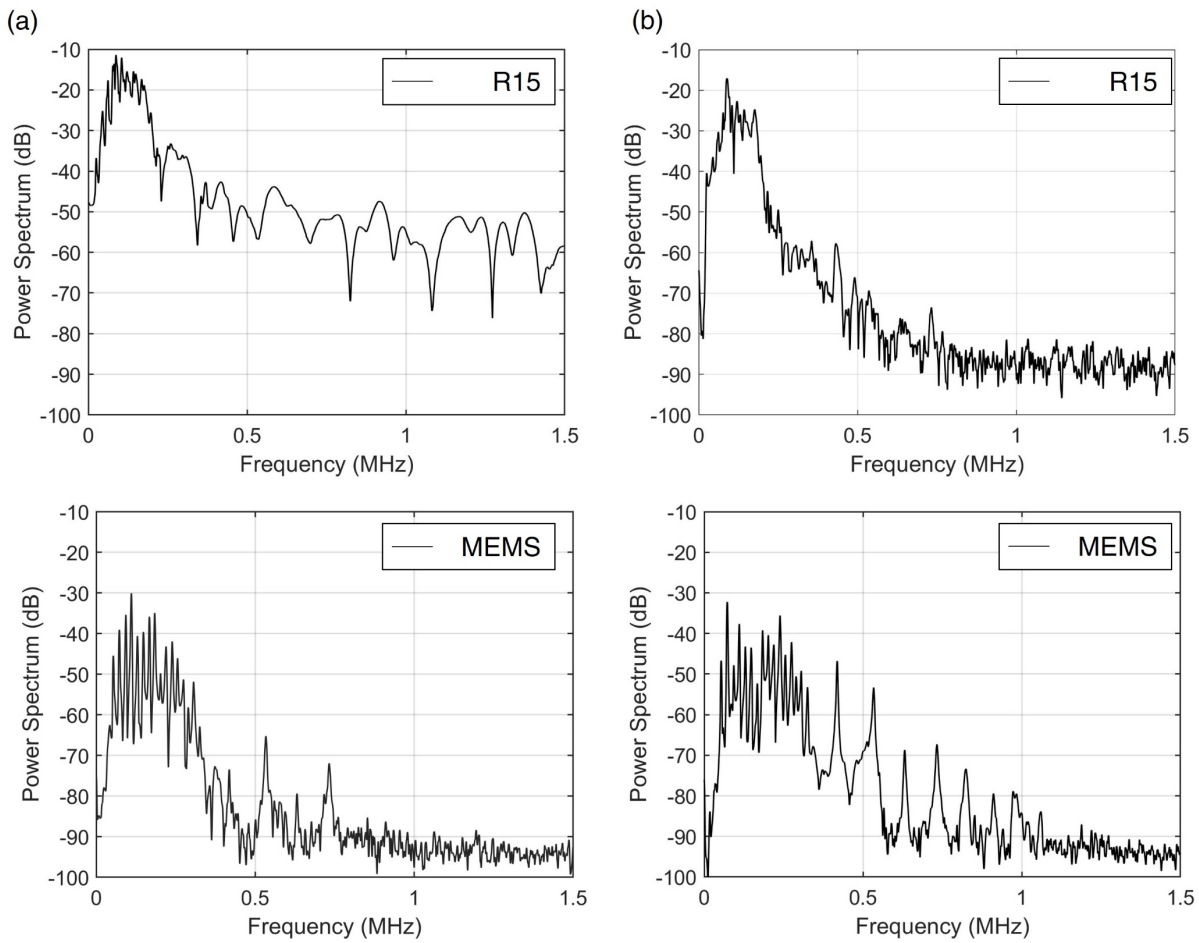

Figure 15: The power spectra of AE signals recorded by R15 and MEMS when the PLB simulations are conducted on (a) the top surface, parallel plane as the sensor area (PLB-1), and (b) the bottom surface, orthogonal to the sensor area (PLB-2).

6 Conclusions

This paper describes the design, fabrication, and characterization of a multifrequency MEMS acoustic emission sensor composed of sixteen resonators tuned to distinct frequencies and connected in parallel. Individual characterization of each resonator was performed using a layout with separate metal pads, while the parallel connection behavior was analyzed using a layout with all resonators connected as a single channel at the die level. Impedance measurements revealed that the parallel connection increased stray capacitance, leading to a slight shift in the resonant frequency. Numerical models demonstrated that low-frequency resonators were more sensitive than high-frequency sensors due to the selection of the same mass for each resonator but different beam lengths. A customized packaging was developed to improve sensor coupling and reduce electronic noise, resulting in improved robustness for field testing. AE simulation experiments showed that while the MEMS AE sensor was about 10 dB less sensitive at the resonant

frequency than a bulky commercial AE sensor, it could simultaneously detect multiple frequencies with higher amplitudes. The study suggests that using a ceramic PCB instead of a plastic PCB in the packaging could further improve coupling loss. In this study, the sensor housing is specifically designed for a single channel, aligning with the objective of capturing AE signals across a wide range of frequencies. However, to enhance the capabilities of the system, the design will incorporate a multiplexer using CMOS on MEMS technology at the device level as future work. By integrating a multiplexer, the size of the package can be further reduced while accommodating multiple channels within the same sensor housing. Furthermore, an impedance matching circuit will be incorporated between the sensor and the data acquisition system. This circuit will be designed to minimize signal loss and optimize the transfer of signal between the sensor and the electronics. The applications of MEMS AE sensors that are embedded into structures and the integration with the modal analyses in guided mediums such as plates and pipes will be investigated as future work.

Acknowledgment

This work was performed with support from the National Science Foundation under Award No. IIP 2016444 entitled "PFI-TT: Multi-Frequency Acoustic Device for Rapid Infrastructure Damage Diagnostics." The support from the sponsoring organization is gratefully acknowledged. Any opinions, findings, conclusions, or recommendations expressed in this paper are those of the authors and do not necessarily reflect the views of the organization acknowledged above.

References

Appalla, A., ElBatanouny, M. K., Velez, W., & Ziehl, P. (2016). Assessing Corrosion Damage in Posttensioned Concrete Structures Using Acoustic Emission. *Journal of Materials in Civil Engineering*, *28(2)*, 4015128. https://doi.org/10.1061/(ASCE)MT.1943-5533.0001389.

Avila Gomez, A. E. (2017). Development MEMS Acoustic Emission Sensors. *ProQuest Dissertations Publishing*.

Behnia, A., Chai, H. K., & Shiotani, T. (2014). Advanced structural health monitoring of concrete structures with the aid of acoustic emission. *Construction & Building Materials, 65*, 282–302. https://doi.org/10.1016/j.conbuildmat.2014.04.103.

Bhugra, H., & Piazza, G. (Eds.). (2017). *Piezoelectric MEMS resonators* (p. 103). New York, NY, USA: Springer International Publishing.

Birjis, Y., Swaminathan, S., Nazemi, H., Raj, G. C. A., Munirathinam, P., Abu-Libdeh, A., & Emadi, A. (2022). Piezoelectric Micromachined Ultrasonic Transducers (PMUTs): Performance Metrics, Advancements, and Applications. *Sensors*, *22*(23), 9151.

Butaud, P., Le Moal, P., Bourbon, G., Placet, V., Ramasso, E., Verdin, B., & Joseph, E. (2020). Towards a better understanding of the CMUTs potential for SHM applications. *Sensors and Actuators. A. Physical., 313*, 112212. https://doi.org/10.1016/j.sna.2020.112212.

Chare, C., Gijsenbergh, P., Jeong, Y., Heremans, P., Cheyns, D., & Genoe, J. (2022). Electromechanical equivalent circuit model for axisymmetric PMUTs with elastic boundary conditions. *Journal of Microelectromechanical Systems*, *31(3),* 457-472.

Chen, X., Qu, M., Zhu, K., & Xie, J. (2021). Dual-Frequency Piezoelectric Micromachined Ultrasonic Transducers via Beam-Membrane Coupled Structure. *IEEE Electron Device Letters, 42*(6), 919–922. https://doi.org/10.1109/LED.2021.3075853.

Chopra, A. (2006). Dynamics of Structures, 3rd edition, Pearson.

Chun, D.-M., Sato, M., & Kanno, I. (2013). Precise measurement of the transverse piezoelectric coefficient for thin films on anisotropic substrate. *Journal of Applied Physics, 113*(4), 044111. https://doi.org/10.1063/1.4789347.

Cowen, A., Hames, H., Gulkh, K., & Hardy, B. (2014). *PiezoMUMPs Design Handbook* (Vol. 1.3 ed). MEMSCAP Inc.

Dausch, D., Castellucci, J., Chou, D., & von Ramm, O. (2008). Theory and operation of 2-D array piezoelectric micromachined ultrasound transducers. *IEEE Transactions on Ultrasonics, Ferroelectrics, and Frequency Control, 55(11)*, 2484–2492. https://doi.org/10.1109/TUFFC.956.

Dubois, M.-A., & Muralt, P. (1999). Measurement of the effective transverse piezoelectric coefficient e31,f of AlN and Pb(Zrx,Ti1−x)O3 thin films. *Sensors and Actuators. A. Physical., 77*(2), 106–112. https://doi.org/10.1016/S0924-4247(99)00070-9.

Dubois, M.-A., & Muralt, P. (1999). Properties of aluminum nitride thin films for piezoelectric transducers and microwave filter applications. *Applied Physics Letters, 74*(20), 3032–3034. https://doi.org/10.1063/1.124055.

Feng, G.-H., & Tsai, M.-Y. (2010). Acoustic emission sensor with structure-enhanced sensing mechanism based on micro-embossed piezoelectric polymer. *Sensors and Actuators. A. Physical., 162*(1), 100–106. https://doi.org/10.1016/j.sna.2010.06.019.

Gillan, E. G. (2013). 1.31-Precursor Chemistry–Group 13 Nitrides and Phosphides (Al, Ga, and In). In *Comprehensive Inorganic Chemistry II* (pp. 969-1000). Elsevier Ltd. https://www.rsc.org/periodic-table/element/14/silicon (RSC Si).

Jia, L., Shi, L., Liu, C., Yao, Y., Sun, C., & Wu, G. (2021). Design and characterization of an aluminum nitride-based MEMS hydrophone with biologically honeycomb architecture. *IEEE Transactions on Electron Devices, 68*(9), 4656-4663.

Jung, J., Lee, W., Kang, W., Shin, E., Ryu, J., & Choi, H. (2017). Review of piezoelectric micromachined ultrasonic transducers and their applications. *Journal of Micromechanics and Microengineering, 27*(11), 113001. https://doi.org/10.1088/1361-6439/aa851b.

Kabir, M., Kazari, H., & Ozevin, D. (2018). Piezoelectric MEMS acoustic emission sensors. *Sensors and Actuators. A. Physical*, 279, 53–64. https://doi.org/10.1016/j.sna.2018.05.044.

Karimian, S. F., & Modarres, M. (2021). Acoustic emission signal clustering in CFRP laminates using a new feature set based on waveform analysis and information entropy analysis. *Composite Structures, 268*, 113987. https://doi.org/10.1016/j.compstruct.2021.113987.

Kawasaki, Y., Fukui, S., & Fukuyama, T. (2022). Phenomenological process of rebar corrosion in reinforced concrete evaluated by acoustic emission and electrochemical noise. *Construction & Building Materials, 352*, 128829. https://doi.org/10.1016/j.conbuildmat.2022.128829.

Kumar, A., Prasad, M., Janyani, V., & Yadav, R. P. (2019). Fabrication and Annealing Temperature Optimization for a Piezoelectric ZnO Based MEMS Acoustic Sensor. *Journal of Electronic Materials, 48*(9), 5693–5701. https://doi.org/10.1007/s11664-019-07383-4.

Lee, J., Lee, K.-R., Eovino, B. E., Park, J. H., Liang, L. Y., Lin, L., Yoo, H.-J., & Yoo, J. (2021). A 36-Channel Auto-Calibrated Front-End ASIC for a pMUT-Based Miniaturized 3-D Ultrasound System. *IEEE Journal of Solid-State Circuits, 56*(6), 1910–1923. https://doi.org/10.1109/JSSC.2021.3049560.

Liu, T.-H. (2018). Testing and Packaging for MEMS Acoustic Emission Sensors. *ProQuest Dissertations Publishing.*

Liu, W., He, L., Wang, X., Zhou, J., Xu, W., Smagin, N., Toubal, M., Yu, H., Gu, Y., Xu, J., Remiens, D., & Ren, J. (2019). 3D FEM Analysis of High-Frequency AlN-Based PMUT Arrays on Cavity SOI. *Sensors (Basel, Switzerland), 19*(20), 4450. https://doi.org/10.3390/s19204450.

Liu, Z., Yoshida, S., Horsley, D. A., & Tanaka, S. (2022). Fabrication and characterization of row-column addressed pMUT array with monocrystalline PZT thin film toward creating ultrasonic imager. *Sensors and Actuators. A. Physical, 342*, 113666. https://doi.org/10.1016/j.sna.2022.113666.

Lu, Y., Tang, H., Fung, S., Wang, Q., Tsai, J. M., Daneman, M., Boser, B. E., & Horsley, D. A. (2015). Ultrasonic fingerprint sensor using a piezoelectric micromachined ultrasonic transducer array integrated with complementary metal oxide semiconductor electronics. *Applied Physics Letters, 106*(26), 263503–. https://doi.org/10.1063/1.4922915.

Luo, G.-L., Kusano, Y., & Horsley, D. A. (2021). Airborne Piezoelectric Micromachined Ultrasonic Transducers for Long-Range Detection. *Journal of Microelectromechanical Systems, 30*(1), 81–89. https://doi.org/10.1109/JMEMS.2020.3037298.

Matsushima, T., Kanno, I., & Wasa, K. (2012). 8 - Thin Film MEMS. *Handbook of Sputter Deposition Technology* (Second Edition, pp. 559–596). Elsevier Inc. https://doi.org/10.1016/B978-1-4377-3483-6.00008-5.

Nastro, A., Ferrari, M., Rufer, L., Basrour, S., & Ferrari, V. (2022). Piezoelectric MEMS Acoustic Transducer with Electrically-Tunable Resonant Frequency. *Micromachines (Basel), 13*(1), 96. https://doi.org/10.3390/mi13010096.

Ozevin, D. (2020). MEMS Acoustic Emission Sensors. *Applied Sciences, 10*(24), 8966. https://doi.org/10.3390/app10248966.

Ozevin, D., Greve, D. W., Oppenheim, I. J., & Pessiki, S. P. (2006). Resonant capacitive MEMS acoustic emission transducers. *Smart Materials and Structures, 15*(6), 1863–1871. https://doi.org/10.1088/0964-1726/15/6/041.

Qu, M., Chen, X., Zhu, K., Guo, X., & Xie, J. (2022). Beam-Membrane Coupled Piezoelectric Micromachined Ultrasonic Transducers with Enhanced Transmitting Sensitivity. *Micromachines (Basel), 13*(3), 423. https://doi.org/10.3390/mi13030423.

Saboonchi, H., & Ozevin, D. (2013). MEMS acoustic emission transducers designed with high aspect ratio geometry. *Smart Materials and Structures, 22*(9), 95006–1–14. https://doi.org/10.1088/0964-1726/22/9/095006,

Sause, M. G. R., & Horn, S. (2010). Simulation of Acoustic Emission in Planar Carbon Fiber Reinforced Plastic Specimens. *Journal of Nondestructive Evaluation, 29*(2), 123–142. https://doi.org/10.1007/s10921-010-0071-7.

Sause, M. G. R., Gribov, A., Unwin, A. R., & Horn, S. (2012). Pattern recognition approach to identify natural clusters of acoustic emission signals. *Pattern Recognition Letters, 33*(1), 17–23. https://doi.org/10.1016/j.patrec.2011.09.018.

Wang, H., Chen, Z., Yang, H., Jiang, H., & Xie, H. (2020). A Ceramic PZT-Based PMUT Array for Endoscopic Photoacoustic Imaging. *Journal of Microelectromechanical Systems, 29*(5), 1038–1043. https://doi.org/10.1109/JMEMS.2020.3010773.

Wang, X.-B., He, L.-M., Ma, Y.-C., Liu, W.-J., Xu, W.-J., Ren, J.-Y., Riaud, A., & Zhou, J. (2021). Development of Broadband High-Frequency Piezoelectric Micromachined Ultrasonic Transducer Array. *Sensors (Basel, Switzerland), 21*(5), 1823. https://doi.org/10.3390/s21051823.

Wang, Z., Miao, J., & Zhu, W. (2008). Micromachined ultrasonic transducers and arrays based on piezoelectric thick film. *Applied Physics. A: Materials Science & Processing*, *91*(1), 107–117. https://doi.org/10.1007/s00339-007-4369-y.

Wright, A. P. (2009). A multi-axis capacitive MEMS sensor system for acoustic emission sensing. *ProQuest Dissertations Publishing.*